Non-Planar Overlapped Inductors Applied to Domestic Induction Heating Appliances

***Abstract*—Domestic induction heating appliances are evolving from surfaces with three to five fixed cooking areas to flexible cooking zones. These are able to adapt to a number of vessels of any size and shape by using multiple coils. Some state-of-the-art induction systems make use of overlapped inductors in two layers, which combine the high efficiency of large inductors with the high flexibility of small adjacent coils. The main drawback of this concept is the unequal distance between different coils and the vessel, which implies that each coil presents a different impedance depending on its layer. This paper presents an induction system conformed by non-planar inductors. These inductors are designed in such a way that they can be assembled in overlapping structures while preserving equivalence among them, i.e. they all present the same impedance. The paper includes the FEM modeling of the non-planar coil, an analysis on the conductor's losses and an experimental verification.**

***Index Terms*—Induction heating, flexible surface, non-planar inductor, overlapping inductors.**

I. Introduction

DOMESTIC induction heating appliances are experiencing ascendant sales across Europe and Asia. The provided advantages as fast heating, advanced control and safety, make of this technology the choice of many users [1]. As a consequence, these appliances are in constant evolution in the seek of new features and improvements.

Domestic induction cooktops are fed from the mains, and make use of a rectifier and a filter to generate a dc bus. Then, an inverter, usually a resonant series half-bridge [2]–[5], is used to generate a medium-high frequency voltage (20 kHz - 100 kHz) which causes an ac current to flow through the inductor. The alternating magnetic field produced by the inductor heats up the pot due to Joule effect and hysteresis losses.

Conventional cookers consist of three to five independent circular cooking areas. Such structure sets limits in the number, shape and size of the pots. In order to overcome the limits, coils arrays are an extended solution [1], [6], [7]. Such arrangements increase the flexibility allowing the user to place several pots of any shape at any point of the active surface . On the other hand, this solution implies the use of a large number of reduced-size inductors, decreasing the energy transfer efficiency and increasing the production cost of the system. An example of a totally active domestic cooktop is shown in Fig. 1a.

Since the efficiency largely depends on the inductor diameter, implementations with partially overlapped coils were considered for low profile wireless power transfer systems [8]. An example of this configuration is shown in Fig. 1b. This alternative provides a comparable load coverage resolution keeping the size of the inductors. However, in these configurations the distance to the load is different for the inductors placed in different layers leading to different operation conditions. This concept was evaluated for domestic cooktops [9]–[11] proving the viability of the system and showing good results in terms of efficiency. On the other hand, inductors in different layers showed different impedances. This results in the need of a complex control and uneven heat distribution in the pot.

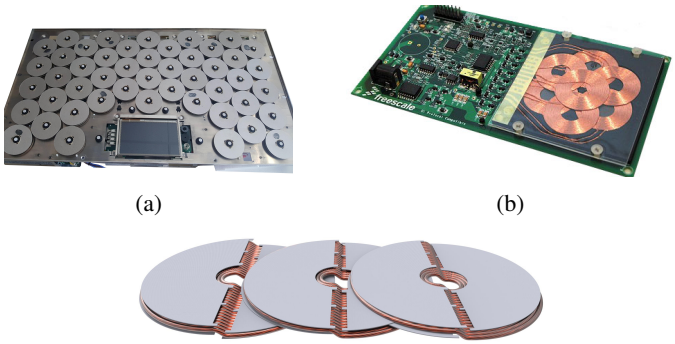

Fig. 1: Configurations of flexible energy transfer systems. (a) Matrix of reduced-size inductors for induction heating. (b) Overlapped planar inductors in three layers for contactless charging. Courtesy of Wireless Power Consortium. (c) Proposed non-planar overlapped configuration.

In this work the use of non-planar inductors is proposed in order to overlap large inductors while preserving the equivalence among them. The proposed system is shown in Fig. 1c. This solution uses non-planar inductors which occupy space in two different layers at the same time, in contrast with the configurations shown in Fig. 1a and Fig. 1b, in which one inductor occupies space in one single layer. The main objective of the proposed configuration is to achieve equivalent inductors which operate in the same conditions, and therefore, the same inverter can be used to power any of them indifferently.

Firstly, in Section II the non-planar inductor will be modeled. The aim of the electromagnetic model is to substitute the inductor-pot system by its equivalent impedance. In Section III, the prototype is presented and the main experimental results will be discussed verifying the electromagnetic model.

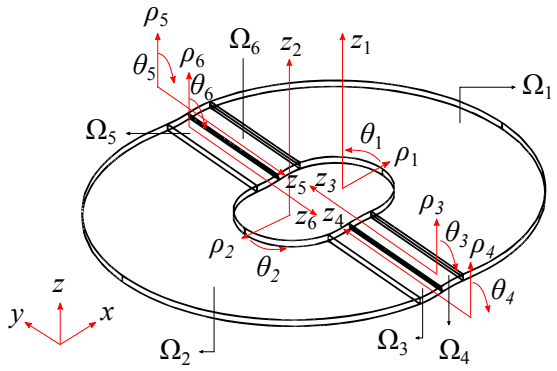

(a)

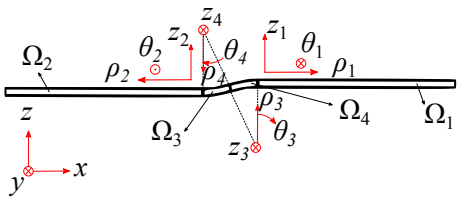

(b)

Fig. 2: Inductor model geometry. (a) 3D view. (b) Side view.

Finally, in Section IV, the suitability of non-planar overlapped inductors for domestic induction heating appliances will be discussed and conclusions will be drawn.

II. Electromagnetic Modeling

A. Inductor geometry definition

The inductor model is composed of 6 revoluted rectangles conforming a non planar structure. Each of them is considered a different domain Ω_i and has an associated cylindrical coordinate system $\{\rho_i, \theta_i, z_i\}$, where $i = 1, 2...6$. The revolution is performed around the z_i axis. Fig. 2 depicts the inductor geometry, its domains and their associated coordinate systems.

B. Current density definition

The inductor is modeled as a current density flowing though the described geometry. The current density $J(x, y, z)$ can be defined as the driven current I multiplied by the number of turns n and divided by the coil cross section S_{coil}. The current density is defined in every domain i in its azimuthal direction $\hat{\theta}_i$. The trajectory is graphically represented in Fig. 3.

$$\vec{J}(x, y, z) = \frac{nI}{S_{coil}}\hat{\theta}_i\,, \quad \{x, y, z\} \in \Omega_i \tag{1}$$

C. Equivalent impedance calculation

Induction systems are commonly modeled by their equivalent impedance, Z, composed by the series connection of a resistance R and an inductance L. This equivalent impedance of the system can be calculated by Ohm's Law as $Z = V/I$,

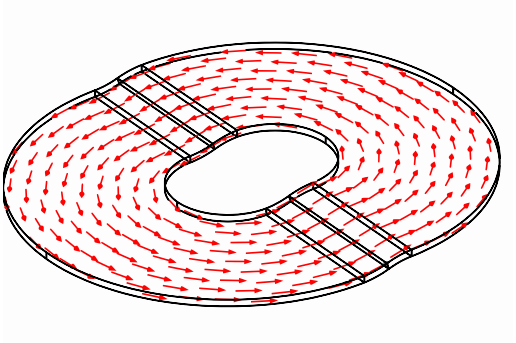

Fig. 3: Current density trajectory along the non-planar inductor.

where I is the imposed current and V is the generated voltage. This voltage, is obtained by calculating the line integral of the electric field $\vec{E}$ along the trajectory of the inductor, which can be decomposed in the 6 different domains. Accordingly, the total voltage is the sum of the partial voltages generated in each domain Ω_i of volume V_i. Therefore, considering an inductor with n turns, the voltage can be expressed as:

$$V = \sum_{i=1}^{6} \frac{-n}{S_{coil}} \iiint_{\Omega_i} \vec{E}\cdot\hat{\rho}_i + \vec{E}\cdot\hat{z}_i + \vec{E}\cdot\hat{\theta}_i \; dV_i \tag{2}$$

Taking into acount that the electric field follows the same trajectory as the current, and this is defined in the $\hat{\theta}$ direction of each cylindrical coordinate system, $\hat{\theta}_i$, the electric field is in every domain perpendicular to the unitary vectors $\hat{\rho}_i$ and $\hat{z}_i$. Removing these terms and applying Ohm's Law, the induction impedance can be written as:

$$Z = \frac{-n}{I \cdot S_{coil}} \sum_{i=1}^{6} \iiint_{\Omega_i} \vec{E}\cdot\hat{\theta}_i \; dV_i \tag{3}$$

The series resistance and inductance are straightforwardly calculated as $R = \mathrm{Re}(Z)$ and $L = \mathrm{Im}(Z)/\omega$ respectively.

D. Winding losses calculation

The inductor is wound with litz wire; a multi-stranded wire in which strands rotate their positions ideally occupying all possible positions periodically along the cable. Such cabling structure is widely used in medium-high frequency applications due the reduced dc, skin and proximity losses in the winding [12]–[15]. On one hand, dc and skin losses are produced by the current flowing through the cable, caused by an externally applied voltage. On the other hand, proximity losses are caused by induced currents produced by and alternating magnetic field, which is usually caused by the inductor itself. These power losses can be expressed in terms of resistances per unit length for one single conductor, $R_{dc,skin,u.l.}$ and $R_{prox,u.l.}$. Moreover, the proximity losses caused by orthogonal components of the magnetic field, H, were proven to be decoupled [16]. As a consequence, the resistance caused by transversal field to the conductor, $R_{prox,t,u.l.}$, and the resistance produced by longitudinal field to the conductor,

$R_{prox,l,u.l.}$, can be calculated separately, i.e. $R_{prox,u.l.} = R_{prox,t,u.l.} + R_{prox,l,u.l.}$.The analytical expressions of these resistances were obtained in [17] .

$$R_{dc,skin,u.l.} = \frac{1}{\pi r_0^2 \sigma} \Phi_{dc,skin}(r_0/\delta) \tag{4}$$

$$R_{prox,t,u.l.} = \frac{4\pi}{\delta} \Phi_{prox}(r_0/\delta) |H_t|^2 \tag{5}$$

$$R_{prox,l,u.l.} = \frac{2\pi}{\delta} \Phi_{prox}(r_0/\delta) |H_l|^2 \tag{6}$$

where r_0 is the strand radius, σ is the conductor electrical conductivity, δ is the skin depth, H_t is the transversal magnetic field, H_l is the transversal magnetic field and $\Phi_{dc,skin}$ and Φ_{prox} are functions including the geometric and frequency dependences. Their analytical expressions where also inferred in [16], [17] and written in terms of Bessel functions, J_0 and J_1 of order 0 and 1 respectively.

$$\Phi_{cond}(r_0/\delta) = \Re e \left((j-1) \frac{r_0}{\delta} \frac{J_0\left((j-1) r_0/\delta\right)}{J_1\left((j-1) r_0/\delta\right)} \right) \tag{7}$$

$$\Phi_{prox}(r_0/\delta) = \Re e \left(j \left(\frac{r_0}{\delta}\right)^2 \frac{J_2\left((j-1) r_0/\delta\right)}{J_0\left((j-1) r_0/\delta\right)} \right) \tag{8}$$

By integration of the resistances per unit length in the cable length, l_w, the winding resistance can be obtained. In the case of dc and skin losses, the integral is immediate. Moreover, considering that the inductor is the parallel connection of n_s strands, the dc and skin resistance of the winding is given by:

$$R_{dc,skin} = \frac{l_w}{n_s \pi r_0^2 \sigma} \Phi_{dc,skin}(r_0/\delta), \tag{9}$$

where the length of the cable is the volume V_{coil} divided by the cross-section multiplied by the number of turns:

$$l_w = n \frac{V_{coil}}{S_{coil}} = \frac{n}{S_{coil}} \sum_{i=1}^{6} \iiint_{\Omega_i} dV_i \tag{10}$$

On the other hand, proximity losses depend on the transversal and longitudinal magnetic field. These take place in every turn and strand adding a $n \cdot n_s$ factor:

$$R_{prox,t} = n \cdot n_s \cdot \frac{4\pi}{\sigma} \Phi_{prox}(r_0/\delta) \left\langle \left|\bar{H}_t\right|^2 \right\rangle \tag{11}$$

$$R_{prox,l} = n \cdot n_s \cdot \frac{2\pi}{\sigma} \Phi_{prox}(r_0/\delta) \left\langle \left|\bar{H}_l\right|^2 \right\rangle \tag{12}$$

Where $\left\langle \left|\bar{H}_t\right|^2 \right\rangle$ and $\left\langle \left|\bar{H}_l\right|^2 \right\rangle$ are the averages of the squared transversal and longitudinal fields respectively. As the conductors are directed in the $\hat{\theta}_i$ direction of each Ω_i domain, the longitudinal component of the field coincides with the azimuthal component and the transversal field is the vector sum of the radial and axial components:

$$\left\langle \left|\bar{H}_l\right|^2 \right\rangle = \frac{1}{V_{coil}} \sum_{i=1}^{6} \iiint_{\Omega_i} \left(\vec{H} \cdot \hat{\theta}_i\right)^2 dV_i \tag{13}$$

$$\left\langle \left|\bar{H}_t\right|^2 \right\rangle = \frac{1}{V_{coil}} \sum_{i=1}^{6} \iiint_{\Omega_i} \left(\vec{H} \cdot \hat{\rho}_i\right)^2 + \left(\vec{H} \cdot \hat{z}_i\right)^2 dV_i \tag{14}$$

The total resistance of the winding, R_w is given by the sum of the dc and skin resitance and the proximity resistance,

$$R_w = R_{dc,skin} + R_{prox,t} + R_{prox,l}. \tag{15}$$

E. Multi-coil system

The described design is intended to be implemented in a coil array, and therefore, two or more inductors may be activated simultaneously. In this case the coupling between them has to be considered. In a n-coil system, this can be done by relating the voltage and current in the coils by the impedance matrix [18]–[20]:

$$\begin{bmatrix} V_1 \\ \vdots \\ V_j \\ \vdots \\ V_n \end{bmatrix} = \begin{bmatrix} Z_{11} & \cdots & Z_{1k} & \cdots & Z_{1n} \\ \vdots & \ddots & \vdots & \iddots & \vdots \\ Z_{j1} & \cdots & Z_{jk} & \cdots & Z_{jn} \\ \vdots & \iddots & \vdots & \ddots & \vdots \\ Z_{n1} & \cdots & Z_{nk} & \cdots & Z_{nn} \end{bmatrix} \begin{bmatrix} I_1 \\ \vdots \\ I_k \\ \vdots \\ I_n \end{bmatrix} \tag{16}$$

where V_j represents the voltage of coil j and I_k represents the current through coil k. The impedance matrix is composed of self-impedances and coupling impedances: the self-impedances are placed at the diagonal positions of the matrix and relate the voltage in a coil to the current flowing through itself. The coupling impedances are placed at non-diagonal positions and relate the voltage induced in a coil by the current flowing through a neighboring coil.

The terms of the impedance matrix can be obtained from the simulations reformulating Equation 3 as:

$$Z_{jk} = \frac{-n}{I_k \cdot S_{coil,j}} \sum_{i=1}^{6} \iiint_{\Omega_{ji}} \vec{E} \cdot \hat{\theta}_{ji} \; dV_{ji}, \tag{17}$$

where $S_{coil,j}$ represents the cross section of coil j, Ω_{ji} is the i domain of the j coil, V_{ji} is its volume, and $\hat{\theta}_{ji}$ is the azimuthal unitary vector of its associated coordinate system. Note that n simulations are needed. Only one coil is excited in each of the simulations, i.e. when I_k is set to 1 A, the rest of the coils are set to 0 A. This step allows the calculation of the k^{th}-column of the impedance matrix.

III. Prototyping and experimental verification

The proposed system consists on 3 aligned partially overlapped inductors generating a flexible cooking area of 430 mm x 180 mm. The coils are powered by 2 half-bridge inverters [21]. The coils to be activated are selected by means of two relays, allowing to operate two overlapping inductors simultaneously. This is schematically represented in Fig. 4.

The design of the inductor was based on the method detailed in Section II including in the simulation ferrite bars

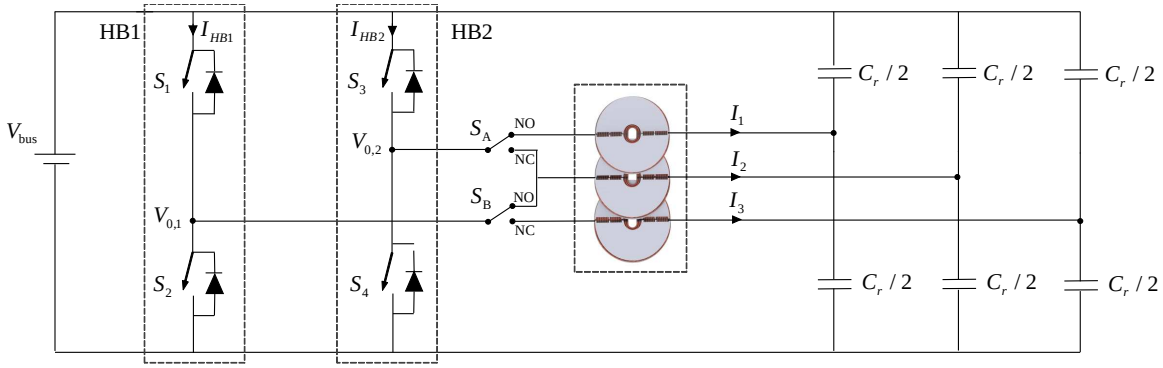

Fig. 4: Proposed topology with 2 half-bridges supplying power to 1 or 2 loads.

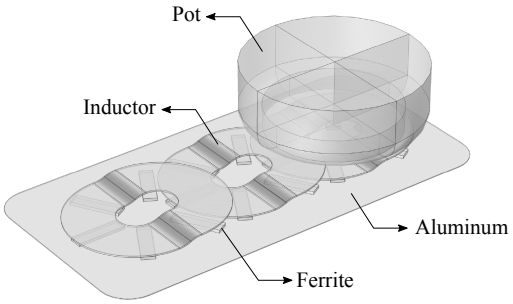

Fig. 5: Simulation model.

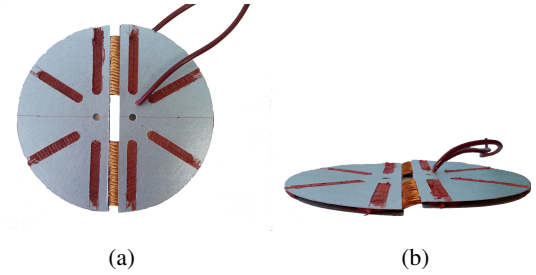

Fig. 6: Prototype. (a) Top view. (b) Side view.

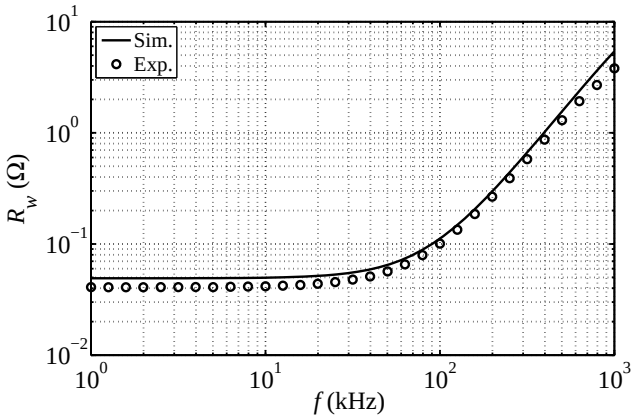

Fig. 7: Winding resistance. Calculated resistance in solid line (Eq. 15). Experimental characterization in circles.

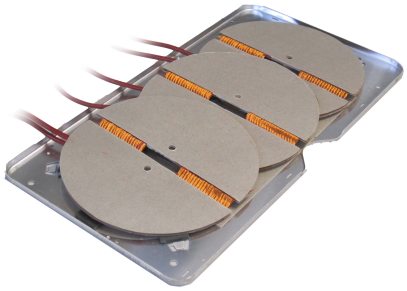

Fig. 8: Final arrangement conforming a flexible induction surface.

which act as flux concentrator, an aluminum shielding tray and the pot made of ferromagnetic steel. The developed simulation model is shown in Fig. 5.

The inductor was designed to supply a maximum power of 3000 W to the load and operate between 25 kHz and 70 kHz connected to a series resonant half-bridge inverter. According to the impedance model, these specifications lead to a coil of 19 turns and a resonant capacitor of 800 nF. The coils were wound with copper litz wire of 140 strands of 0.2 mm.

A. Small signal characterization

Firstly, the non-planar coil model was verified in small signal. For this purpose, one single inductor was measured by an *Agilent E4980A* LCR Meter set to 10 mA. The loss resistance is measured with air as surrounding media (unloaded inductor). Fig. 7 compares the calculated winding resistance R_w (Equation 15) with the measured values. The measured resistance is in good agreement with the calculations.

Then, the 3 overlapped inductors were assembled as shown in Fig. 8. The system was characterized in small signal in order to verify the multi-coil model. A ferromagnetic vessel was placed on the coils fully covering all the inductors. When all inductors are equally covered, the self-impedances of each of them are equal, and coupling impedances between adjacent inductors are also the same. Furthermore, inductors 1 and 3 have a significant distance in between so the related coupling

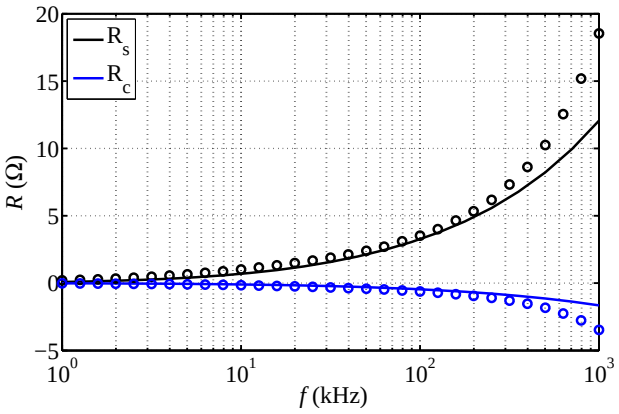

(a)

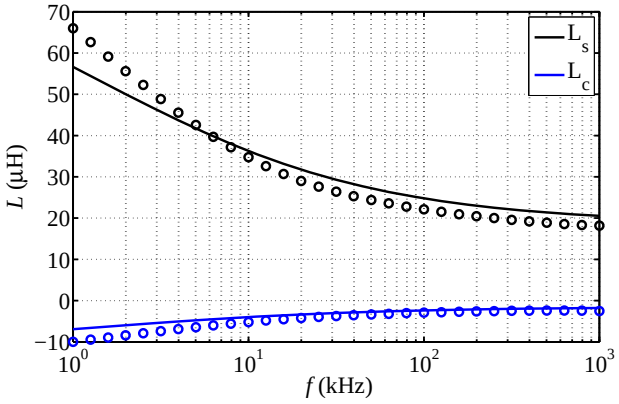

(b)

Fig. 9: Small signal impedance terms when the coils are loaded with a ferromagnetic vessel. Simulation results in solid line. Measurements in circles. (a) Resistance. (b) Inductance.

terms for these coils are almost null and can be neglected. Under equal load conditions, the matrix $\mathbf{Z}$ can be simplified to:

$$\mathbf{Z} = \begin{bmatrix} Z_{11} & Z_{12} & Z_{13} \\ Z_{21} & Z_{22} & Z_{23} \\ Z_{31} & Z_{32} & Z_{33} \end{bmatrix} = \begin{bmatrix} Z_s & Z_c & 0 \\ Z_c & Z_s & Z_c \\ 0 & Z_c & Z_s \end{bmatrix}, \quad (18)$$

where $Z_s = R_s + j\omega L_s$ represents self-impedance and $Z_c = R_c + j\omega L_c$ denotes coupling impedance. In Fig. 9 the simulated impedances are compared to the measured impedances for the final arrangement which is composed by the aluminum plane, ferrites and a ferromagnetic steel as load.

B. Large signal characterization

The multi-coil system was tested in real working conditions. Both inverters were powered by *Xantrex XDC 300-40* dc source and the signals were registered by a *Textronix DPO 7354* Oscilloscope.

In first place, the coils in the corners were activated while the central coil was in open circuit. This test shows the independent activation of two identical inductors when they

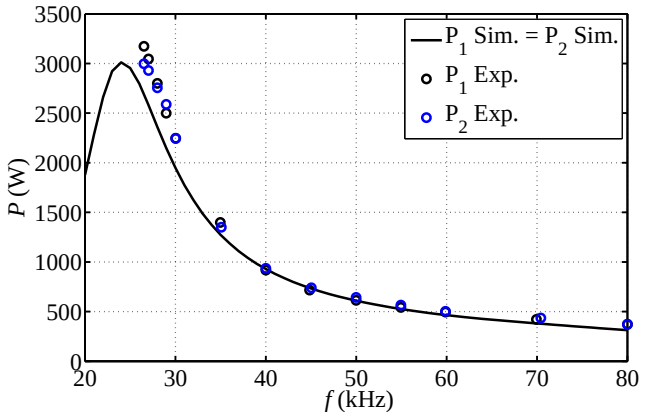

Fig. 10: Power with respect to switching frequency. Calculated curve in solid line. Measurements in circles.

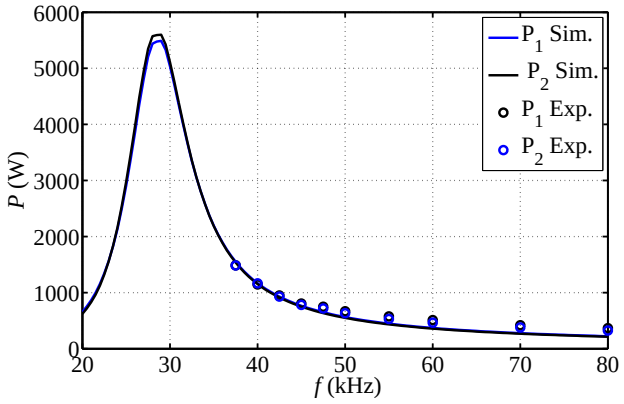

(a)

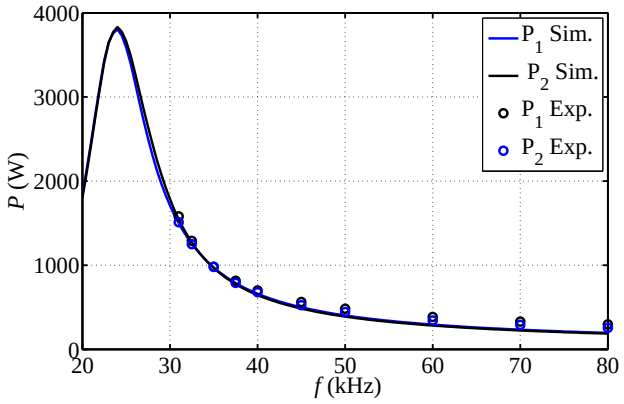

(b)

Fig. 11: Power curves for (a) phase-shift 0° and (b) phase-shift 180°. Simulation results in solid line. Measurements in circles.

are uncoupled. As aimed, the inductors present the same behavior as can be seen in their power curves (Fig. 10).

In the second place, two neighboring inductors were activated simultaneously. As follows from the previous model, the operation of the coils depends on the phase-shift between the inductors. In this case, up to 1600 W were delivered by each inductor to make a total of 3200 W in

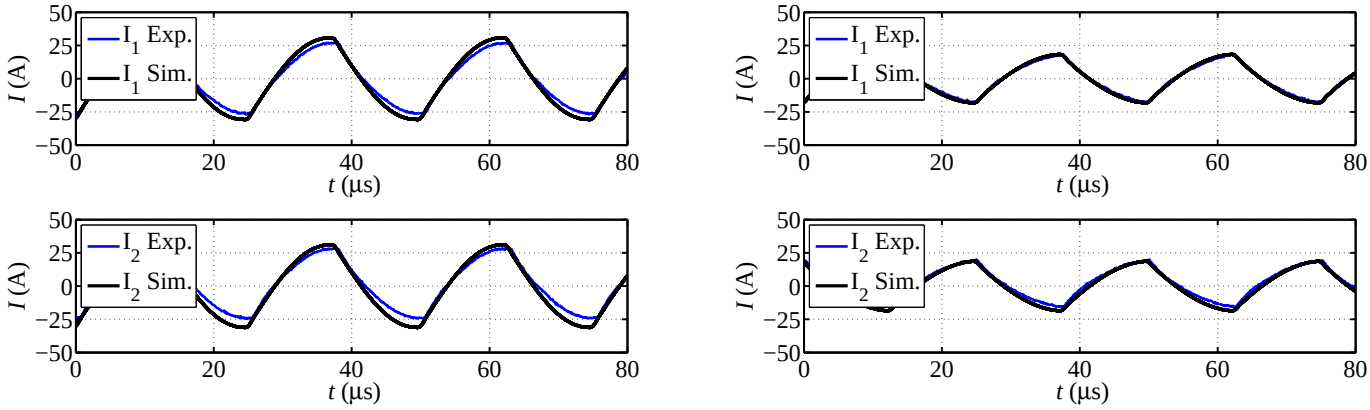

(a) (b)

Fig. 12: Power curves for (a) phase-shift 0° and (b) phase-shift 180°. Simulation results in solid line. Measurements in circles.

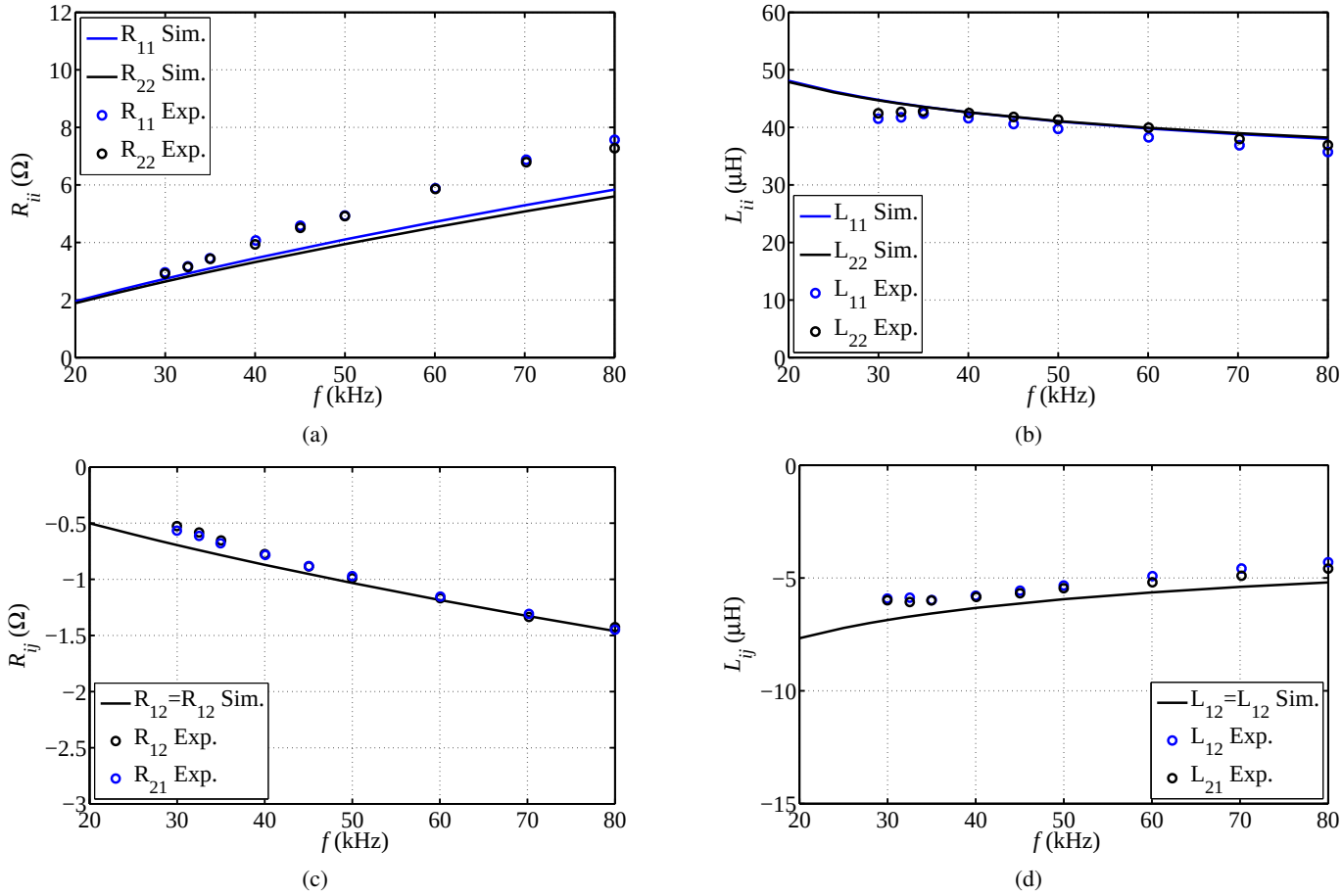

(a) (b) (c) (d)

Fig. 13: Power curves for (a) phase-shift 0° and (b) phase-shift 180°. Simulation results in solid line. Measurements in circles.

the pot. The most representative cases are presented in Fig. 11.

Moreover, the currents through the inductors are consistent with the simulations. Fig. 12 shows, as an example, the current waveforms when the inverters are operated at 40 kHz with a duty cycle of 0.5.

The impedance terms in eq. (18), Z_{11}, Z_{22}, Z_{12}, and Z_{21}, can be extracted from the current and voltage waveforms by approximating these waveforms by their first harmonic. The comparative is shown in Fig. 13. Note that due to the large dependence of ferromagnetic materials behavior on the excitation level, the large signal impedance differ significantly from the small signal impedance shown earlier in Fig. 9.

As can be extracted from the previous figures, the

inductors behave identically, i.e. their impedances are equal and therefore, the currents through them and the delivered powers are the same. This provides several advantages with respect to other systems, which make use of different inductors [21], [22] or equal inductors placed at different distances from the pot [9]. Firstly, both inverters can be employed to supply power to different inductors with no further considerations since these are exchangeable. In the second place, identical resonance capacitors can be used, ensuring the same resonant frequency. Additionally, the voltage to be supported by the capacitors is the same.

The non-planar overlapped structure also presents benefits when two inductors are activated simultaneously. When two unequal coils are activated at the same time, they supply different powers generating an uneven heat distribution [9], [23]. Specific strategies are necessary to mitigate this problem. Since the non-planar coils deliver the same power, a good heat distribution in the base of the pot is ensured [24]. On the other hand, the main drawback of this structure is the increased constructive complexity.

IV. Conclusion

In this paper the concept of non-planar overlapped inductors has been evaluated. The structure was designed pursuing the equivalence among inductors, i.e. achieving inductors with the same impedances and power curves.

Firstly, a FEM simulation model was developed. The model is based on defining the 3D current trajectory and obtaining the electric and magnetic fields, from which the impedance and the loss resistance can be obtained by means of analytical expressions. The model has been applied to a multi-coil system, introducing the effect of the coupling between the coils and reflecting the influence of the phase-shift.

The simulations have been experimentally verified on a prototype. The prototype consists on three inductors that can be activated by means of two inverters. The system operates achieving equal impedances and power curves. This implies several advantages in terms of industrialization, component standardization, system simplicity and performance. On the other hand, constructive complexity is increased. The simulations are consistent with the experimental result and the system performance is satisfactory.

References

[1] O. Lucía, J. Acero, C. Carretero, and J. Burdío, "Induction heating appliances: Toward more flexible cooking surfaces," *Industrial Electronics Magazine, IEEE*, vol. 7, pp. 35–47, Sept 2013.

[2] H. Koertzen, J. Van Wyk, and J. Ferreira, "Design of the half-bridge, series resonant converter for induction cooking," in *Power Electronics Specialists Conference, 1995. PESC '95 Record., 26th Annual IEEE*, vol. 2, pp. 729–735 vol.2, Jun 1995.

[3] F. Forest, S. Faucher, J.-Y. Gaspard, D. Montloup, J.-J. Huselstein, and C. Joubert, "Frequency-synchronized resonant converters for the supply of multiwinding coils in induction cooking appliances," *Industrial Electronics, IEEE Transactions on*, vol. 54, pp. 441–452, Feb 2007.

[4] A. Namadmalan, "Universal tuning system for series-resonant induction heating applications," *IEEE Transactions on Industrial Electronics*, vol. 64, pp. 2801–2808, April 2017.

[5] T. Mishima, C. Takami, and M. Nakaoka, "A new current phasor-controlled zvs twin half-bridge high-frequency resonant inverter for induction heating," *IEEE Transactions on Industrial Electronics*, vol. 61, pp. 2531–2545, May 2014.

[6] C. Carretero, R. Alonso, J. Acero, and J. M. Burdio, "Optimized 4-coil inductor system arrangement for induction heating appliances," in *IECON 2015 - 41st Annual Conference of the IEEE Industrial Electronics Society*, pp. 004948–004952, Nov 2015.

[7] L. C. Meng, K. W. E. Cheng, and S. L. Ho, "Multicoils design for induction cookers with applying switched exciting method," *IEEE Transactions on Magnetics*, vol. 48, pp. 4503–4506, Nov 2012.

[8] J. Achterberg, E. Lomonova, and J. de Boeij, "Coil array structures compared for contactless battery charging platform," *Magnetics, IEEE Transactions on*, vol. 44, pp. 617–622, May 2008.

[9] J. Serrano, J. Acero, I. Lope, C. Carretero, and J. M. Burdio, "A flexible cooking zone composed of partially overlapped inductors," *IEEE Transactions on Industrial Electronics*, vol. PP, no. 99, pp. 1–1, 2018.

[10] W. X. Zhong, X. Liu, and S. Y. R. Hui, "A novel single-layer winding array and receiver coil structure for contactless battery charging systems with free-positioning and localized charging features," *IEEE Transactions on Industrial Electronics*, vol. 58, pp. 4136–4144, Sept 2011.

[11] S. A. Mirbozorgi, H. Bahrami, M. Sawan, and B. Gosselin, "A smart multicoil inductively coupled array for wireless power transmission," *IEEE Transactions on Industrial Electronics*, vol. 61, pp. 6061–6070, Nov 2014.

[12] C. Sullivan and R. Zhang, "Analytical model for effects of twisting on litz-wire losses," in *Control and Modeling for Power Electronics (COMPEL), 2014 IEEE 15th Workshop on*, pp. 1–10, June 2014.

[13] C. Sullivan, "Optimal choice for number of strands in a litz-wire transformer winding," *Power Electronics, IEEE Transactions on*, vol. 14, pp. 283–291, Mar 1999.

[14] H. Hamalainen, J. Pyrhonen, J. Nerg, and J. Talvitie, "Ac resistance factor of litz-wire windings used in low-voltage high-power generators," *Industrial Electronics, IEEE Transactions on*, vol. 61, pp. 693–700, Feb 2014.

[15] J. Ferreira, "Improved analytical modeling of conductive losses in magnetic components," *Power Electronics, IEEE Transactions on*, vol. 9, pp. 127–131, Jan 1994.

[16] C. Carretero, J. Acero, and R. Alonso., "TM-TE decomposition of power losses in multi-stranded litz-wires used in electronic devices," *Progress In Electromagnetics Research*, vol. 123, pp. 83–103, December 2012.

[17] J. Acero, R. Alonso, J. Burdío, L. Barragán, and D. Puyal, "Frequency-dependent resistance in litz-wire planar windings for domestic induction heating appliances," *Power Electronics, IEEE Transactions on*, vol. 21, pp. 856–866, July 2006.

[18] K. R. Davey and D. Zheng, "Prediction and use of impedance matrices for eddy-current problems," *IEEE Transactions on Magnetics*, vol. 33, pp. 2478–2485, Jul 1997.

[19] W. Hurley and M. Duffy, "Calculation of self and mutual impedances in planar magnetic structures," *Magnetics, IEEE Transactions on*, vol. 31, pp. 2416–2422, Jul 1995.

[20] W. Hurley and M. Duffy, "Calculation of self- and mutual impedances in planar sandwich inductors," *Magnetics, IEEE Transactions on*, vol. 33, pp. 2282–2290, May 1997.

[21] C. Carretero, O. Lucia, J. Acero, and J. M. Burdio, "Computational modeling of two partly coupled coils supplied by a double half-bridge resonant inverter for induction heating appliances," *IEEE Transactions on Industrial Electronics*, vol. 60, pp. 3092–3105, Aug 2013.

[22] F. Sanz, C. Sagues, and S. Llorente, "Induction heating appliance with a mobile double-coil inductor," *IEEE Transactions on Industry Applications*, vol. 51, pp. 1945–1952, May 2015.

[23] F. Sanz, C. Sagues, and S. Llorente, "Power distribution in coupled multiple-coil inductors for induction heating appliances," *IEEE Transactions on Industry Applications*, vol. 52, pp. 2537–2544, May 2016.

[24] C. Carretero, J. Acero, R. Alonso, and J. M. Burdio, "Normal-mode decomposition of surface power distribution in multiple-coil induction heating systems," *IEEE Transactions on Magnetics*, vol. 52, pp. 1–8, Feb 2016.